Chapter 9
LIDAR-Based Turbulence Intensity for Aviation Applications

P.W. Chan

Abstract Turbulence could increase the workload of pilots, and timely provision of turbulence information would be beneficial to aircraft operation. This paper summarises the use of a Doppler Light Detection and Ranging (LIDAR) system to measure turbulence intensity at an operating airport. The cube root of eddy dissipation rate (EDR) is used for representing the turbulence intensity, according to the requirement of the International Civil Aviation Organization (ICAO). The quality of EDR so calculated is established by comparing with the aircraft data. Examples of EDR maps based on conical scans of the LIDAR are presented. The EDR maps so obtained should be useful for aviation operations, and the EDRs calculated from the glide-path scans of the LIDAR may be used for turbulence alerting applications.

9.1 Introduction

Low-level turbulence (below 1600 ft from the elevation of the airport) can be hazardous to landing and departing aircraft. Such turbulence may be measured using high-resolution data available from ground-based anemometers. For instance, following the requirements of the International Civil Aviation Organization (ICAO), 10-m-high anemometers may be set up along the runway with high temporal resolution wind data (down to 1 s) available from such equipment for calculating the turbulence intensity, namely, the cube root of eddy dissipation rate (EDR). These calculated EDRs are useful for monitoring the level of turbulence at the airport area.

However, once airborne, the turbulence the aircraft experiences may be different from that measured at the ground. In that case, remote-sensing meteorological equipment would be useful in providing an estimate of EDR along flight paths. One possible source of EDR comes from microwave weather radars, such as the Terminal Doppler Weather Radar (TDWR) installed at some airports. The

P.W. Chan (✉)
Hong Kong Observatory, Hong Kong, China
e-mail: pwchan@hko.gov.hk

R. Sharman, T. Lane (eds.), *Aviation Turbulence*,
DOI 10.1007/978-3-319-23630-8_9

spectral width measured in the return signal of TDWR might be used to provide an estimate of the turbulence intensity, which could be useful for monitoring the level of turbulence in rainy conditions. For non-rainy weather conditions, such radars might not give persistently good quality signals for weather monitoring purpose.

To monitor the turbulence in such conditions, the Doppler Light Detection and Ranging (LIDAR) systems are used increasingly at the airports around the world. In Hong Kong, the complex terrain can on occasion give rise to turbulent airflow in the airport area. The LIDAR introduced to this airport in 2002 provides very useful information for the depiction of the airflow around the airport, particularly when there is disruption of airflow by nearby terrain. The LIDAR data are used to calculate the EDR, and there are interesting observations of the turbulence intensity in different kinds of weather conditions. The locations of meteorological equipment at the airport in Hong Kong are found in Fig. 9.1.

This chapter focuses on the LIDAR-calculated EDR for airport operations at HKIA. The LIDAR has been used to do glide-path and conical scans, and the

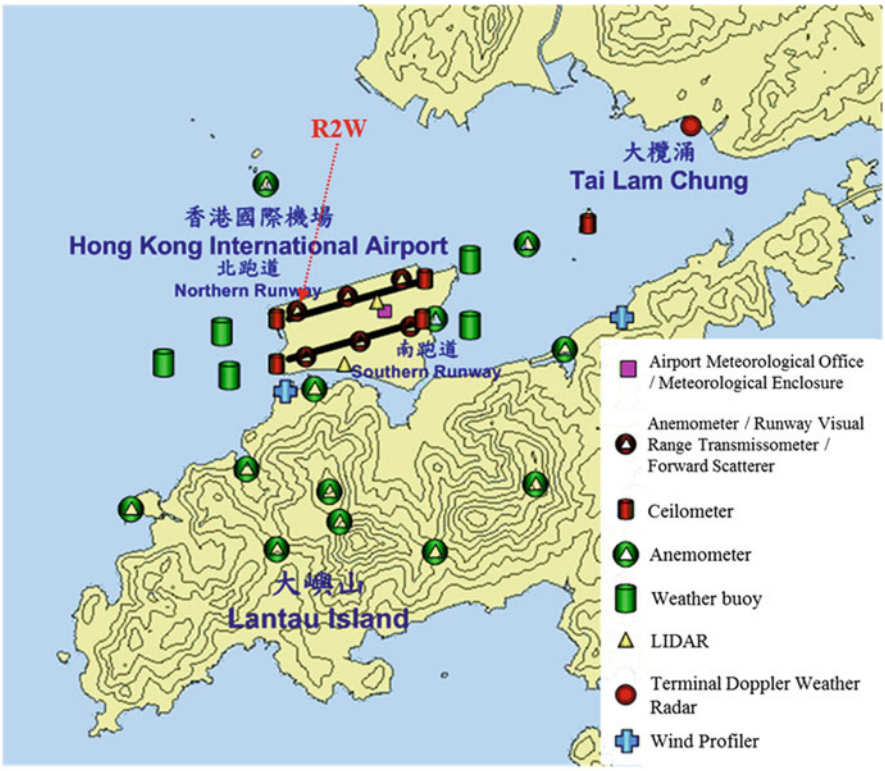

Fig. 9.1 Locations of meteorological equipment at the Hong Kong International Airport. Height contours are in 100 m. The length of the runway is about 3.8 km, which can be used as a length scale of the picture

mathematical formulation of the EDR calculation for such scans is reviewed. It is followed by EDR observations in the airport area for typical cases of terrain-disrupted airflow. The quality of EDR from the LIDAR is then studied by comparison with that obtained from the research aircraft. Application of LIDAR-derived EDR in the alerting of low-level turbulence is discussed, and finally the observations in tropical cyclone (TC) cases are reviewed.

9.2 Calculation of EDR Based on Glide-Path Scans

In the glide-path scan mode, the laser beam of the LIDAR is configured to scan along the oblique line of the glide path in space by orchestrating the azimuthal and elevation motions of the laser scanner. For alerting of wind shear, i.e. significant changes of headwind, only the radial velocity data collected within a confined rectangular block around the glide path are utilised to construct the headwind profile to be encountered by the aircraft (Shun and Chan 2008). In calculating turbulence intensity, all the wind data in the measurement sector of the glide-path scan are considered. The whole measurement sector is divided into a number of overlapping subsectors (each with a size of 10 range gates and 16 azimuth angles, overlapping by 5 range gates and 8 azimuth angles). EDR is calculated in each subsector by adopting a spatial fluctuation method in the structure function approach (Frehlich et al. 2006).

For more accurate determination of the turbulence intensity, azimuthal averaging is minimised by reducing the horizontal rotation speed of the laser beam given the time constraint that the LIDAR is also required to perform other non-glide-path scans for operational purposes. For the current setting of the LIDAR, the gate length Δp is 105 m. Based on results of previous studies (Frehlich 2001; Frehlich and Cornman 2002), $\Delta h/\Delta p$ ($\Delta h =$ range $\times$ azimuthal span) should be much less than 1 so that azimuthal averaging is small compared with the range scale length (averaging along the range gate). For real application, this ratio could be set at a maximum value of 0.2. Taking the maximum range of 10 km for the LIDAR and the data output frequency of 10 Hz from the LIDAR, the azimuthal rate α should be $\Delta h = 10{,}000\ \text{m} \times \alpha \times 0.1\ \text{s} \leq 0.2 \times 105\ \text{m}$, which implies that $\alpha \leq 0.021\ \text{rad s}^{-1}$ or $1.2^\circ\ \text{s}^{-1}$. This provides a realistic value of the upper bound for the azimuthal rate over a small sector considering operational scanning requirements and laser safety consideration. The azimuthal rate of about $0.8^\circ\ \text{s}^{-1}$ has been implemented for the glide-path scans over the arrival runway corridors of HKIA, including the two most used arrival corridors: 07LA (arrival at the north runway of HKIA from the west) and 25RA (arrival at the north runway of HKIA from the east).

Each subsector in the glide-path scanning area has a size of 10 range gates times 16 radials. For a particular scan k, the radial velocity "surface" within this subsector (as a function of range R and azimuth angle θ) is fitted with a plane using the singular value decomposition method. This is essentially the removal of the linear

trend. The velocity fluctuation $\hat{v}'$ at each point in the space (R, θ) is taken to be the difference between the measured radial velocity $\hat{v}$ and the fitted velocity $\overline{v}$ on the plane:

$$\hat{v}'(R,\theta,k) = \hat{v}(R,\theta,k) - \overline{v}(R,\theta,k). \tag{9.1}$$

Both longitudinal and azimuthal structure functions are calculated (Frehlich et al. 2006). The longitudinal structure function is given by:

$$\hat{D}_L(R_1,R_2) = N^{-1}\sum_{\theta,k}\left[\hat{v}'(R_1,\theta,k) - \hat{v}'(R_2,\theta,k)\right]^2 - E(R_1,R_2) \tag{9.2}$$

where the summation is made over all the possible azimuthal angles and scans over 15 min (about 7–8 glide-path scans, with the scan at each runway corridor updated every 2 min or so), and N refers to the total number of entries in the summation. The choice of 15 min is a balance between the collection of sufficient statistics of turbulent eddies moving across the measurement domain (which requires a longer period of time considering the revisit time of 2 min for glide-path scans) and the time required for capturing the stronger turbulence (which requires a shorter period of time because the use of longer period would tend to smooth out the stronger turbulence in the sampling period). The error term E is calculated using the covariance method on the radial velocity difference (Frehlich 2001; Frehlich et al. 2006) by estimation of the covariance values of different azimuthal changes by linear approximation to lag 0:

$$E = \hat{C}(0) - 2\hat{C}(\Delta\theta) + \hat{C}(2\Delta\theta). \tag{9.3}$$

The azimuthal structure function is calculated in a way similar to Eq. (9.2), but the radial velocity difference of two azimuthal angles is considered:

$$\hat{D}_{AZ}(R\cdot\theta_1, R\cdot\theta_2) = N^{-1}\sum_{R,k}\left[\hat{v}'\left(R,\theta_1,{}^1k\right) - \hat{v}'(R,\theta_2,k)\right]^2 - E(R). \tag{9.4}$$

Again, the error term is estimated using the covariance method. The covariance of velocity estimate is:

$$\hat{C}(R,n\Delta\theta) = N^{-1}\sum_{l,k}\hat{v}'(R,l\Delta\theta,k)\times\hat{v}'(R,(l+n)\Delta\theta,k). \tag{9.5}$$

The error term of velocity difference is taken as two times the error of the velocity estimate [hence the factor of 2 at the beginning of the right-hand side of Eq. (9.6)]:

$$E = 2\left(\hat{C}(0) - 2\hat{C}(\Delta\theta) + \hat{C}(2\Delta\theta)\right). \tag{9.6}$$

$EDR^{1/3}$ is determined by fitting the longitudinal or the azimuthal structure function with the theoretical von Kármán model (Frehlich et al. 2006). As an example, the calculation of EDR based on azimuthal structure function is given here.

Let $s = R\ (\theta_1 - \theta_2)$ for two azimuthal angles θ_1 and θ_2. According to Frehlich et al. (2006), for homogeneous von Kármán turbulence over a two-dimensional plane (R, s),

$$D_{\mathrm{AZ}}(R,s) = 2\sigma^2\left[\Lambda(q/L_0) + \Lambda_D(q/L_0)\left(1 - R^2/q^2\right)\right], \tag{9.7}$$

where $q = \left(R^2 + s^2\right)^{1/2}$,

$$\Lambda_D(x) = (0.29627426)x^{4/3}K_{2/3}(x), \tag{9.8}$$

σ^2 is the variance of the radial velocity, L_0 is the outer scale of turbulence, $\Lambda(x)$ is a universal function and $K_{2/3}(x)$ is the modified Bessel function of order 2/3. Since the LIDAR is configured to scan in the azimuthal direction very slowly such that the transverse dimension of the LIDAR sensing volume for each radial velocity estimate is much less than the range resolution of about 105 m, Eq. (9.7) could be simplified to be:

$$D_{\mathrm{AZ}}(s,\sigma,L_0) = 2\sigma^2 G_\theta(s/\Delta p,\mu,\chi), \tag{9.9}$$

where $\mu = (2\ln 2)^{1/2}\Delta p/\Delta r, \chi = \Delta p/L_0$, Δr is the full width at half maximum of the LIDAR sensing volume in range that defines the extent of the illuminated aerosol targets and G_θ is given as Eq. (46) in Frehlich et al. (2006) and repeated below:

$$G_\theta(m,\mu,\chi) = 2\int_0^\infty F(x,\mu)\left[\Lambda\left(\chi\sqrt{m^2+x^2}\right) - \Lambda(\chi x) + \Lambda_D\left(\chi\sqrt{m^2+x^2}\right)m^2/\left(m^2 + x^2\right)\right]\mathrm{d}x,$$

where $F(x,\mu) = \frac{1}{2\sqrt{\pi}\mu}\left\{\exp\left[-\mu^2(x+1)^2\right] + \exp\left[-\mu^2(x-1)^2\right] - 2\exp(-\mu^2x^2)\right\} + \frac{1}{2}\left\{(x+1)\mathrm{Erf}[\mu(x+1)] + (x-1)\mathrm{Erf}[\mu(x-1)] - 2\cdot\mathrm{Erf}(\mu x)\right\}$ and $\mathrm{Erf}(x)$ is the standard error function.

The azimuthal structure function is calculated from the LIDAR's radial velocity and then fitted with the theoretical von Kármán model to give σ^2 and L_0. EDR (also denoted as ε) is given by:

$$\mathrm{EDR} = (0.933668)\frac{\sigma^3}{L_0}. \tag{9.10}$$

The fitting involves the minimization of a cost function to obtain two unknown parameters, namely, the variance of radial velocity and the outer scale of turbulence.

The values calculated from both azimuthal and longitudinal methods are studied in a number of cases of turbulent flow with different intensities, and they are found to be comparable with each other with a correlation coefficient (R^2) reaching 0.9. In the following discussions, only the $EDR^{1/3}$ determined from azimuthal structure function will be used.

The turbulence intensity distribution based on the two-dimensional plan position indicator (PPI) scans is calculated using a similar method.

9.3 Examples of LIDAR-Based Turbulence Intensity

To illustrate the observation of EDR in different kinds of turbulent flow at HKIA, two examples of PPI-based maps are presented in this section.

9.3.1 Springtime Case: 23–25 March 2004

During the morning of 24 March 2004, synoptic-scale high pressure over the south-eastern coast of China brought an easterly airstream to Hong Kong. As shown in the LIDAR's velocity data in the 0° elevation PPI scans (Fig. 9.2a), the wind was mainly from the east, with a slight southerly component. The magnitude of the maximum radial velocity was about 10 m s^{-1}. The $EDR^{1/3}$ calculated from these scans (Fig. 9.2b) was generally small in the vicinity of HKIA at that time, in the order of 0.15 $m^{2/3}$ s^{-1} or less (light and dark blue). There were a few localised regions with higher $EDR^{1/3}$ values. For instance, $EDR^{1/3}$ reached about 0.35 $m^{2/3}$ s^{-1} over a continuous region to the east-northeast of the LIDAR just beyond its blind zone.

Later that day, the wind increased and veered gradually, which resulted in a more southerly component. Accelerated flows emanating from the valleys of Lantau Island became more apparent (Fig. 9.2c). Compared to the situation in the morning, the $EDR^{1/3}$ was generally higher in the vicinity of HKIA (Fig. 9.2d) as a result of higher wind speeds and greater disruption of the southerly airflow by the Lantau terrain. In the evening $EDR^{1/3}$ was on the order of 0.3 $m^{2/3}$ s^{-1} or above within the first 2 km downstream of Lantau Island and gradually decreased northward over the sea. Moreover, the $EDR^{1/3}$ was generally higher (exceeding 0.5 $m^{2/3}$ s^{-1}) just downstream of the Lantau terrain to the west of the LIDAR compared with similar locations to the east of the LIDAR. These regions of higher $EDR^{1/3}$ appear as "flares of red" emanating from the terrain in Fig. 9.2d. The more turbulent airflow in that location may be related to the convergence between the prevailing

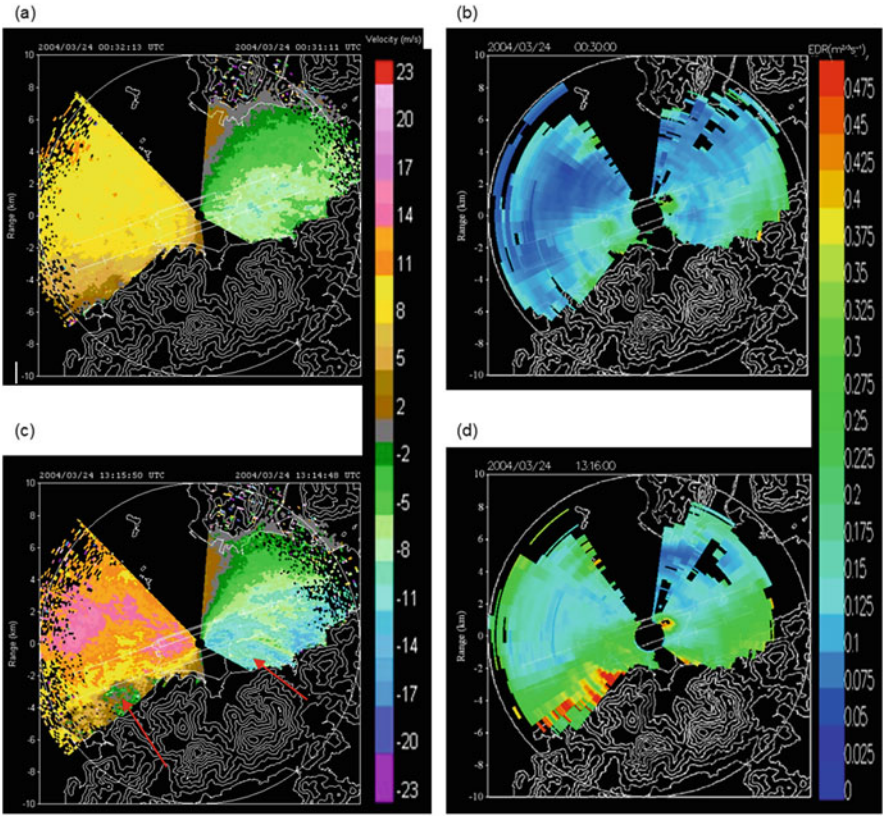

Fig. 9.2 Radial velocity imagery (*left-hand side*) and EDR map (*right-hand side*) obtained from 0° PPI scans of the LIDAR at about 00:30 UTC [(**a**) and (**b**)] and 13:16 UTC [(**c**) and (**d**)] of 24 March 2004. The major valley flows from Lantau Island are indicated by *red arrows* in (**c**). The colour scales of the figures are given on the *right-hand side* of each figure

easterly over HKIA and the southerly valley flow from Lantau Island and the jump/mountain wake in the valley flow (Szeto and Chan 2006).

To examine the quality of the LIDAR-based $EDR^{1/3}$ estimates, we compare them with the $EDR^{1/3}$ values calculated from the wind velocity measurements (at 20 Hz output) of a 3-D sonic anemometer on Lantau Island (see Fig. 9.1 for location). The sonic anemometer was set up at the top of a wind mast of 10 m above the ground. It was located at the top of a small hill having a height of about 166 m above mean sea level.

The $EDR^{1/3}$ calculation method is similar to that used in a past experiment performed on a rather flat area (Chan 2004). However, since the anemometer in this case is mounted on top of a conical hill, the vertical velocity is not always negligible in comparison to the horizontal wind speed. In fact, it is not uncommon to have an upward velocity of several metres per second in strong east to southeasterly winds. Following the common practice, a co-ordinate transformation is applied to the three

components of the wind to align the longitudinal axis with the mean wind direction. The $EDR^{1/3}$ is then calculated using maximum likelihood estimator method (Smalikho 1997). This involves the fast Fourier transform of the time series of the horizontal wind velocity (normally the longitudinal component of the wind is used). Technical details are found in Smalikho (1997).

The scatter plot of the $EDR^{1/3}$ calculated from the vertical velocity data of the sonic anemometer and that from the 1° elevation PPI scans of the LIDAR at the location nearest to the anemometer has been prepared (not shown), with the *y*-intercept set to be zero. The elevation of these PPI scans is chosen because the height of the laser beam at the anemometer's location (137 m AMSL) is close to that of the anemometer itself (176 m AMSL). The plot covers the period 23–25 March 2004. Both LIDAR and anemometer $EDR^{1/3}$ values are determined over 30-min periods. The slope of the least-square linear fit to the data points is close to unity. The correlation coefficient between the two datasets exceeds 0.9, which is considered very high, judging from the fact that the $EDR^{1/3}$ from the sonic anemometer is essentially a point measurement, whereas the corresponding value from the LIDAR represents the turbulence over a much larger area (1 km in range and 20° in azimuth).

Table 9.1 summarises the slopes and correlation coefficients of the least-square linear fits (with *y*-intercepts set to be zero) between the $EDR^{1/3}$ determined from each of the three components of the wind data of the sonic anemometer and that from the 1° elevation PPI scans of the LIDAR. The slopes are close to unity and the correlation coefficients are about 0.9 in all cases. The sonic anemometer is situated at about 5 km from the LIDAR, which is half of the LIDAR's maximum measurement range. From the present results, the effect of velocity averaging of the LIDAR in the longitudinal and transverse dimensions on $EDR^{1/3}$ estimation (Hannon et al. 2005) is not significant, at least at this range from the LIDAR.

The vertical velocity spectrum is obtained from the sonic anemometer, and structure functions are calculated from the LIDAR data for cases of both weak (04:00 local time) and strong turbulence (21:30 local time). For the vertical velocity spectrum, in general the inertial subrange (with a slope of $-5/3$) is well captured. For the structure function, the calculated values generally fit well with the theoretical model. It is noted that the sampling volume of the sonic anemometer and that of the LIDAR is very different. For the sonic anemometer, it is essentially a point in space. For the LIDAR, it has a range span of about 1 km and an azimuthal span of 20 beams. Moreover, the sonic anemometer is close to the ground (10 m above the hilltop), and the LIDAR's laser beam is much higher above ground (at least 50 m above ground for horizontal scans; even higher for 1° elevation scan). The sampling periods for both instruments are 30 min. The $EDR^{1/3}$ value based on sonic anemometer data and that based on LIDAR data could be quite different due to the differences in the sampling volume and the height above ground.

Table 9.1 Slope (m) and correlation coefficient of the least-square linear fit ($y = m \times x$) between the $EDR^{1/3}$ derived from different wind components of the sonic anemometer (y) and that calculated from 1° PPI scan of the LIDAR (x) at the anemometer's location

Wind component of the sonic anemometer to calculate $EDR^{1/3}$	Slope	Correlation coefficient (R)
Vertical	0.9981	0.911
Longitudinal	1.1274	0.903
Transverse	0.9177	0.887

9.3.2 Typhoon Case: 23–27 August 2003

Typhoon Krovanh tracked west-northwestward across the northern part of the South China Sea in late August 2003. It brought east to southeasterly storm-force winds to Hong Kong. For instance, at about 1:30 a.m. of 25 August 2003 (17:30 UTC of 24 August), the 1° elevation PPI scans of the LIDAR show radial velocities close to 20 m s^{-1} in the vicinity of HKIA (Fig. 9.3a). Because of the high humidity, the measurement range of the LIDAR was reduced. There were not much velocity data beyond 8 km or so to the west of the LIDAR.

Similar to the above springtime case, the airflow is more turbulent in the areas just downstream of the Lantau terrain to the west of the LIDAR compared with the corresponding locations east of the LIDAR, as revealed by the presence of many small-scale features (with horizontal dimensions of several hundred metres) in the radial velocity imagery (Fig. 9.3a). This pattern is also confirmed from the EDR map (Fig. 9.3b). Once again, "flares" of high $EDR^{1/3}$ values (around 0.5 $m^{2/3}$ s^{-1}) emanate from the Lantau terrain to the southwest of LIDAR. They are more extensive in size compared to the springtime case and affect almost the whole western approach corridor of the south runway.

The $EDR^{1/3}$ determined from 1° elevation PPI scans of the LIDAR is compared in Table 9.2 with that derived from sonic anemometer winds. Compared to the springtime case, the slopes deviate slightly more from unity and the correlation coefficients are generally smaller, but still reach at least 0.92 and 0.8, respectively. The calculation of $EDR^{1/3}$ in the typhoon case is more challenging because of the limited measurement range of the LIDAR and the missing/erroneous wind data from the sonic anemometer in episodes of heavy rain. Given that, the present comparison results are considered to be satisfactory.

9.4 Comparison with Flight Data

The Observatory regularly obtains flight data from commercial jets and a fixed-wing aircraft operated by the Government Flying Service (GFS). Such data would be useful in the development of turbulence detection algorithms and verification of

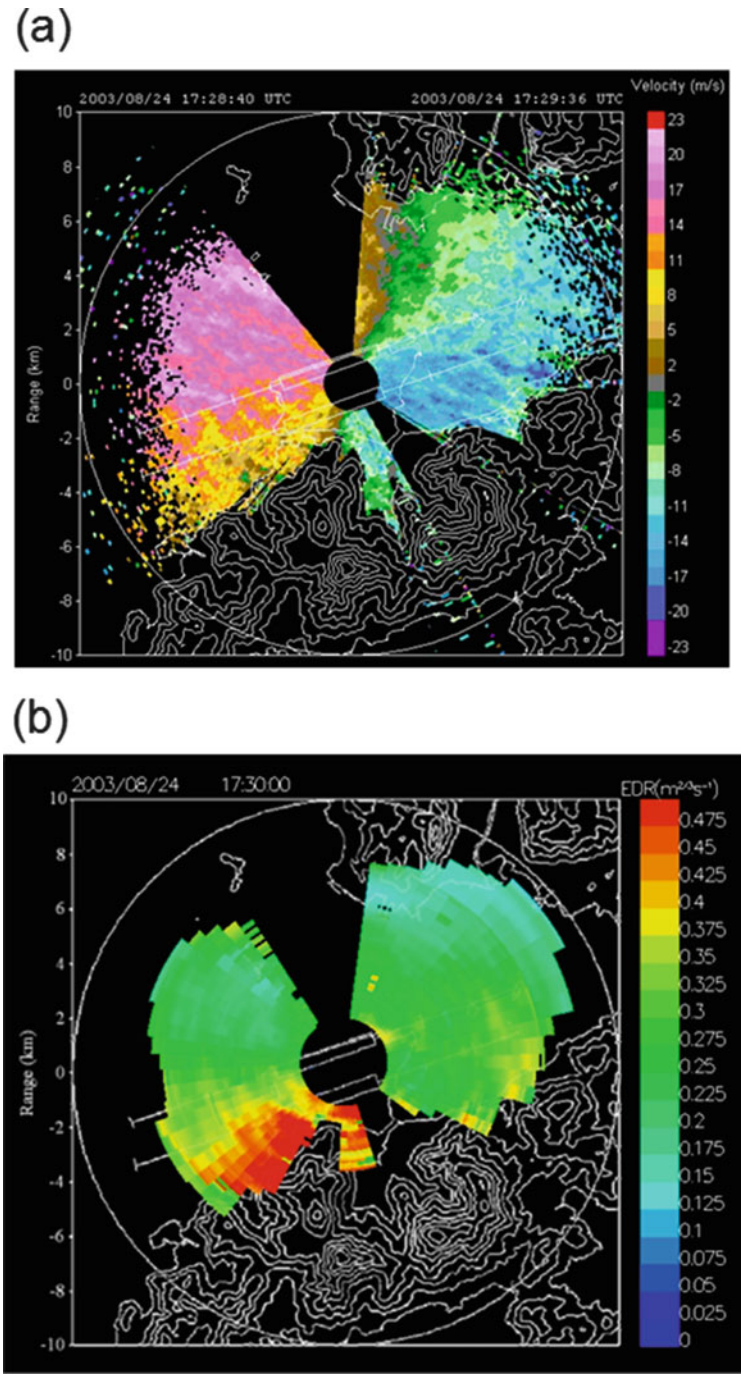

Fig. 9.3 Radial velocity imagery from 1° PPI scan of the LIDAR (**a**) and the EDR map (**b**) at around 17:30 UTC, 24 August 2003. The colour scales of the figures are given on the *right-hand side* of each figure

Table 9.2 Same as Table 9.1, but for the period 23–27 August 2003

Wind component of the sonic anemometer to calculate $EDR^{1/3}$	Slope	Correlation coefficient (R)
Vertical	0.9283	0.851
Longitudinal	0.9881	0.799
Transverse	0.9247	0.839

the turbulence intensity as calculated from different remote-sensing instruments, including the LIDARs. A comparison between headwind data as estimated by LIDAR glide-path scans, and as measured on board an instrumented aircraft of GFS over corridors 07LA and 25RA, is first presented here.

For the GFS fixed-wing aircraft, a high-resolution data probe, capable of measuring horizontal wind components, pressure and humidity at a frequency up to 20 Hz, is installed. Technical specifications of the data probe (AIMMS-20) can be found in Beswick et al. (2008). Data collection flights are regularly carried out (about three times every week) during which the aircraft performs 2–3 take-off/touchdown cycles. With reference to the LIDAR glide-path scanning strategy, elevation angles of 3 and 6° are observed, respectively, for touchdown and take-off motions. Between the months of January and September from 2010 to 2012, a total of 333 (270) measured headwind profiles have been available over 07LA (25RA).

Given the high temporal resolution (20 Hz) of wind data collected by AIMMS-20, some form of data thinning is required for a fair comparison with LIDAR glide-path scans, which come with a line-of-sight resolution of about 100 m. In the current study, the distance d is the distance along the extended centre line of the runway away from the runway threshold of each LIDAR datapoint is first identified, and a corresponding datapoint is extracted from aircraft measurements at the same position d. Spatial location of the two data points would coincide perfectly if they follow the same elevation angle (3° for arrival) as well as touchdown location, here assumed at the runway threshold. In reality this is not always the case. Additional quality control (QC) is therefore implemented by filtering pairs of data points with horizontal distance over 0.25 nautical miles (about 460 m) away from each other.

Figure 9.4 shows the scatter plot of LIDAR-estimated and measured headwinds over corridors 07LA and 25RA. In both cases strong positive correlations can be observed between the two data sources over a wide range of velocities from −10 to +30 knots (about −5 to +15 m s^{-1}). Linear regression gives a slope of 0.88 (0.90) and intercept of 0.29 (0.04) knot with a correlation coefficient R^2 of 0.80 (0.77) over 07LA (25RA), indicating that on average LIDAR values are about 10 % higher than GFS measurements. For both corridors over 90 % of data pairs (histogram not shown) are within 5 knot (2.5 m s^{-1}) from each other.

An algorithm for calculating EDR from AIMMS-20 measurements based on direct fitting of the inertial subrange of the turbulence spectrum, developed by the

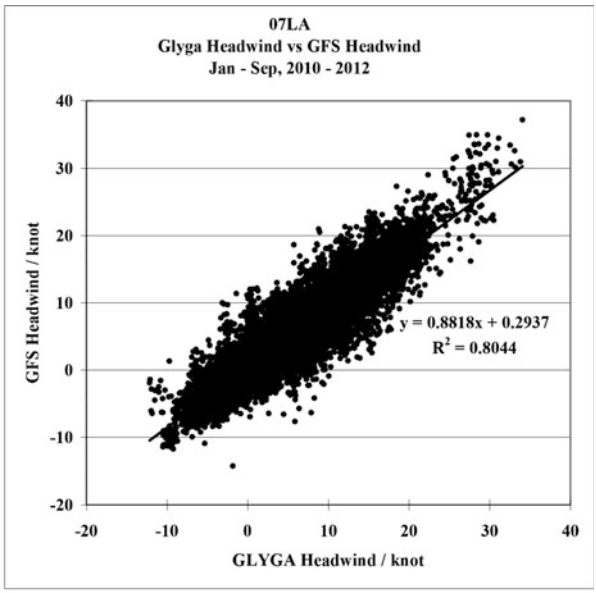

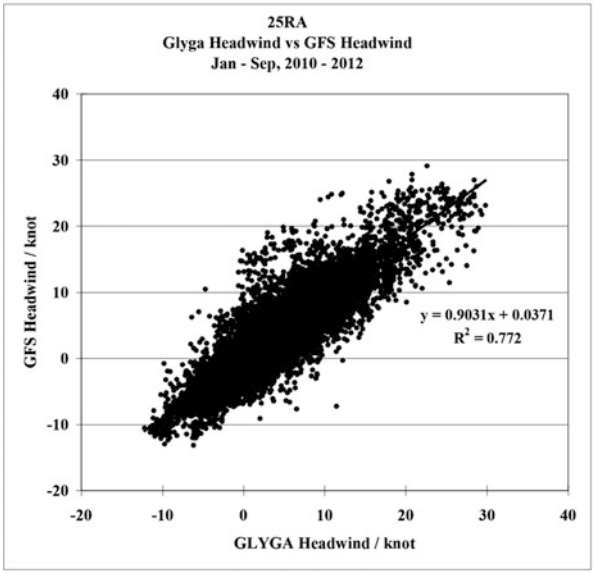

Fig. 9.4 Comparison of headwind measured on board a GFS fixed-wing aircraft during touchdown/take off at HKIA and that from the corresponding LIDAR glide-path scan for corridors 07LA (*top*) and 25RA (*bottom*)

National Aerospace Laboratory and similar to De Bruin and Haverdings (2007), has been available to process data collected during the above GFS flights. Comparison of EDR values derived from LIDAR and flight data are shown in Fig. 9.5, where a positive linear correlation can be observed for runway corridor 07LA.

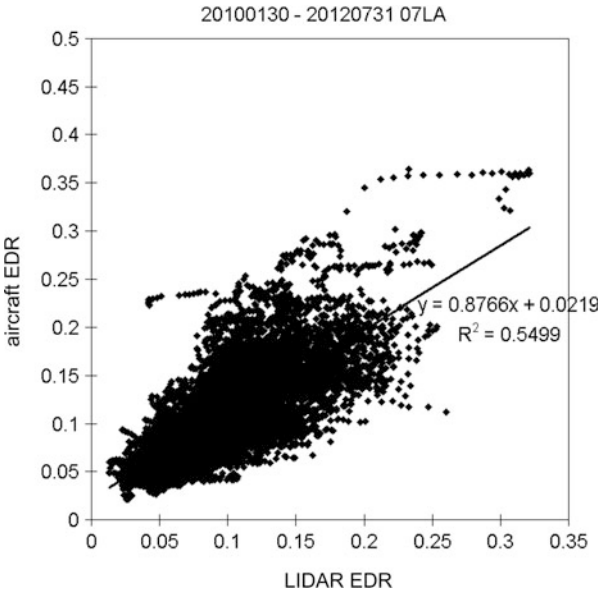

Fig. 9.5 Comparison of EDR between research aircraft and LIDAR for runway corridor 07LA

9.5 Performance on Alerting of Low-Level Turbulence

Having established the correlation between in situ measurements and LIDAR-derived analogues, for both headwinds, and EDR profiles, we now explore the application of EDR profiles for diagnosing low-level turbulence at HKIA.

Following the method described in Sect. 9.2, EDR profiles along aircraft glide paths are calculated at 15-min intervals (available at 00, 15, 30 and 45 min of each hour) for the months of January to September 2008–2012 over arrival corridors 07LA and 25RA of HKIA. These profiles are available at a line-of-sight resolution of about 100 m and cover a distance up to 6–8 km (about 3–4 nautical miles) along the extended centre line of the runway away from the respective runway threshold, depending on meteorological conditions. A threshold-based approach is then applied such that an alert will be triggered whenever a representative value of EDR from the LIDAR-derived profile exceeds a predetermined threshold. Each alert is valid for 15 min and is based on the EDR profile calculated from LIDAR sector/glide-path scans over the previous 15 min (e.g. an alert issued at 11:15 UTC is based on the EDR profile calculated using data between 11:00 and 11:15 UTC and will be valid until 11:30 UTC). In what follows, the use of both the maximum and the median EDR values from each profile as the representative EDR value will be explored.

These alerts are then validated against pilot reports of significant low-level turbulence (intensity of moderate or above) received during the study period. A total of 89 (48) turbulence events have been reported over 07LA (25RA). An event of turbulence is taken as a “hit” if its time of occurrence falls within a 15-min

interval where an EDR-based alert is valid. By applying a range of alert thresholds, overall skill level of the EDR-based alerting method can be assessed using a modified relative operating characteristics (ROC) diagram. The vertical and horizontal axes are, respectively, the percentage of detection (PoD) and the percentage of time on alert (PoTA), defined as:

$$\text{PoD} = \frac{\text{No. of “Hits”}}{\text{Total No. of Pilot Reports}} \times 100\,\% \tag{9.11}$$

$$\text{PoTA} = \frac{\text{No. of Alerts Issued}}{\text{Total No. of 15-min Intervals}} \times 100\,\% \tag{9.12}$$

As with the conventional ROC diagram, high skill level is indicated by proximity to the top-left corner, i.e. high hit rate at low alert duration. Note that by using PoTA as the *x*-axis instead of the false alarm ratio, a perfect forecast with PoD of 100 % and no false alarms will not lie exactly on the top-left corner.

In the resulting ROC diagrams (Fig. 9.6), EDR-based alerts show considerable skill with PoD around 90 % (80 %) at PoTA of 10 % for 07LA (25RA). For both corridors, a slight gain in PoD is obtained by issuing alerts using the median EDR value (2–3 % for 07LA, 5–10 % for 25RA) while keeping PoTA constant. Also included for comparison is the performance of the HKO winds hear and turbulence warning system (WTWS), currently in operation at HKIA, which is characterised by a moderate PoD of 50.6 % (44.4 %) at a very low alert duration of 0.24 % (0.64 %) for 07LA (25RA) over the period 2008–2012 (October to December included). Comparable performance can be obtained from the EDR-based approach using a higher alert threshold, with PoD and PoTA of 47.2 and 0.56 % for 07LA and 54.2 and 1.0 % for 25RA.

The application of LIDAR-derived EDR profiles can be illustrated in the following case. On 22 June 2011, passage of Tropical Storm Haima across the northern part of the South China Sea was responsible for gale force winds both offshore and in Hong Kong. Interactions of low-level southeasterly flows with the Lantau Mountains led to disturbed winds around HKIA. At 22 UTC, a pilot on board an A330 aircraft landing from the west on corridor 07LA reported an encounter of “moderate turbulence”. Despite a positive offset as well as a lack of some fine-scale features, the LIDAR profile corresponds well to the EDR values calculated using the quick access recorder (QAR) data measured on board, which gave a maximum of 0.39 $m^{2/3}\ s^{-1}$ at a similar location.

9.6 Summary and Conclusions

In this chapter, the formulation of LIDAR-derived EDR has been reviewed. It is based on the structure function approach using two calculation methods, namely, azimuthal structure function and longitudinal structure function, and is found to

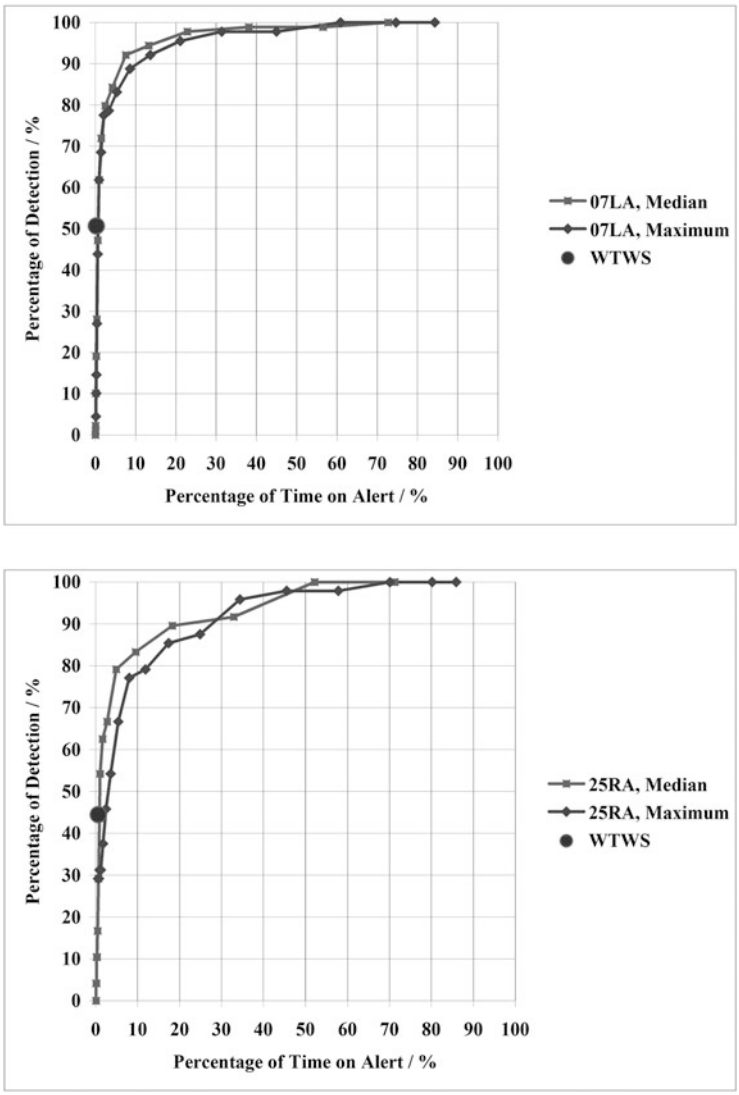

Fig. 9.6 Threshold-based performance of low-level turbulence alerting on corridors 07LA (*top*) and 25RA (*bottom*) at HKIA using LIDAR-derived EDR along glide paths over January to September 2008–2012. Alerts are issued in 15-min intervals either based on the median (*median*, *grey*) or maximum (*maximum*, *black*) values from each EDR profile. The performance of the operational wind shear and turbulence warning system of HKO ("WTWS", *dot*) is included for comparison

give comparable results based on the LIDAR measurements at HKIA. An alternative approach is to use the spectrum width of the LIDAR signal return, but there may be background noise in the equipment (e.g. electronic noise) that needs to be removed, and the calculation of EDR from this approach is not so trivial.

The structure function approach may be applied to two kinds of scanning data of the LIDAR, namely, the glide-path scans and the PPI scans. They have been implemented in real time at HKIA and serve different purposes. The glide-path-scan-based EDR can be used to construct the EDR profile, similar to the headwind profile obtained from this kind of scan, and such profiles may be used to alert the aircraft on the possibility of encountering significant turbulence. On the other hand, the PPI-scan-based EDR gives an overview of the distribution of turbulence intensity over the airport area and could be useful in the understanding and monitoring of turbulence associated with terrain-disrupted airflow, sea breeze fronts and gust fronts associated with thunderstorms.

These two kinds of EDR information are studied in detail later in the chapter. The PPI scans are used to review the overall pattern of EDR in two examples of terrain-disrupted airflow, namely, in springtime easterly to southeasterly flow in stable boundary layers and in turbulent flow associated with TCs. In contrast, glide-path-scan EDRs are used to illustrate the accuracy of the LIDAR-based EDR by comparison with the EDR obtained from a research aircraft. The LIDAR-based EDRs and aircraft-based EDRs are found to have good correlations, illustrating the usefulness of the former in the monitoring of turbulence in the airport area.

The performance of LIDAR-based EDR in the alerting of low-level turbulence is then studied by comparisons with pilot reports of turbulence encounters. Though the sample size of pilot reports is relatively small, the skill of the LIDAR-based EDR is demonstrated using ROC curves.

Looking into the future, the EDR formulation may be applied to the short-range LIDAR data, which are used for monitoring wind shear and turbulence associated with buildings, which are much smaller in spatial scale. The matter is still being actively pursued in Hong Kong and would be reported in future publications.

References

Beswick, K.M., Gallagher, M.W., Webb, A.R., Norton, E.G., Perry, F.: Application of the Aventech AIMMS20AQ airborne probe for turbulence measurements during the convective storm initiation project. Atmos. Chem. Phys. **8**, 5449–5463 (2008)

Chan, P.W.: Measurement of eddy dissipation rate by a mini-sodar for aviation application: comparison with tower measurement. In: Proceedings of the 11th Conference on Aviation, Range, and Aerospace Meteorology, American Meteorological Society, Massachusetts (on-line proceedings) (2004)

De Bruin, A.C., Haverdings, H.: Validation of an eddy dissipation rate calculation method, based on flight data recording data. NLR-CR-2007-540, National Aerospace Laboratory, Amsterdam (2007)

Frehlich, R.G.: Estimation of velocity error for Doppler lidar measurements. J. Atmos. Oceanic Technol. **18**, 1628–1639 (2001)

Frehlich, R.G., Cornman, L.: Estimating spatial velocity statistics with coherent Doppler Lidar. J. Atmos. Oceanic Technol. **19**, 355–366 (2002)

Frehlich, R.G., et al.: Measurements of boundary layer profiles in an urban environment. J. Appl. Meteorol. Climatol. **45**, 821–837 (2006)

Hannon, S.M., Pelk, J.V., Benda, P.: Autonomous Doppler Lidar wind and aerosol measurements for Pentagon Shield. In: Proceedings of the 2nd Symposium on Lidar Atmospheric Applications, American Meteorological Society, California (on-line proceedings) (2005)

Shun, C.M., Chan, P.W.: Applications of an infrared Doppler Lidar in detection of wind shear. J. Atmos. Oceanic Technol. **25**, 637–655 (2008)

Smalikho, I.N.: Accuracy of turbulent energy dissipation rate estimation from wind velocity temporal spectrum. Atmos. Oceanic Opt. **10**, 559–563 (1997)

Szeto, K.C., Chan, P.W.: High resolution numerical modelling of windshear episodes at the Hong Kong International Airport. In: Proceedings of the 12th Conference on Aviation, Range, and Aerospace Meteorology, American Meteorological Society, Georgia (on-line proceedings) (2006)